Physics of the Earth and Planetary Interiors 206–207 (2012) 51–66

Contents lists available at SciVerse ScienceDirect

Physics of the Earth and Planetary Interiors

journal homepage: www.elsevier.com/locate/pepi

Numerical modelling of convection interacting with a melting and solidification front: Application to the thermal evolution of the basal magma ocean

M. Ulvrová [a,*], S. Labrosse [a,b], N. Coltice [a,b], P. Råback [c], P.J. Tackley [d]

[a] Laboratoire de Géologie de Lyon, Université de Lyon, Université Lyon 1, Ecole Normale Supérieure de Lyon, CNRS, Lyon, France
[b] Institut Universitaire de France, France
[c] CSC – IT Center for Science, Espoo, Finland
[d] Institute of Geophysics, Department of Earth Sciences, ETH Zürich, Switzerland

ARTICLE INFO

Article history:
Received 22 December 2011
Received in revised form 7 June 2012
Accepted 22 June 2012
Available online 20 July 2012
Edited by Mark Jellinek

Keywords:
Melting
Solidification
Stefan problem
Phase change
Moving boundary
Convection
Core–Mantle dynamics

ABSTRACT

Melting and solidification are fundamental to geodynamical processes like inner core growth, magma chamber dynamics, and ice and lava lake evolution. Very often, the thermal history of these systems is controlled by convective motions in the melt. Computing the evolution of convection with a solid–liquid phase change requires specific numerical methods to track the phase boundary and resolve the heat transfer within and between the two separate phases. Here we present two classes of method to model the phase transition coupled with convection. The first, referred to as the moving boundary method, uses the finite element method and treats the liquid and the solid as two distinct grid domains. In the second approach, based on the enthalpy method, the governing equations are solved on a regular rectangular grid with the finite volume method. In this case, the solid and the liquid are regarded as one domain in which the phase change is incorporated implicitly by imposing the liquid fraction f_L as a function of temperature and a viscosity that varies strongly with f_L. We subject the two modelling frameworks to thorough evaluation by performing benchmarks, in order to ascertain their range of applicability. With these tools we perform a systematic study to infer heat transfer characteristics of a solidifying convecting layer. Parametrized relations are then used to estimate the super-isentropic temperature difference maintained across a basal magma ocean (BMO) (Labrosse et al., 2007), which happens to be minute (< 0.1 K), implying that the Earth's core must cool at the same pace as the BMO.

1. Introduction

Solidification and melting dynamics have always attracted a lot of attention, particularly for practical applications: industrial engineering including metal processing, solidification of castings, or welding, as well as environmental and food engineering. Yet, changing phase state – tightly linked with mechanics – also plays a fundamental role in Earth and planetary evolution. Crystallization in magma chambers (Brandeis and Jaupart, 1986; Brandeis and Marsh, 1989) as well as inner core growth (Alboussière et al., 2010) are examples of geodynamic processes that have shaped the state of our planet.

A recent model suggests that after formation of the core, a basal magma ocean (BMO) was formed at the bottom of Earth's mantle and has slowly solidified since (Labrosse et al., 2007; Coltice et al., 2011). Remnants may be seismically observed as partially molten regions at the core mantle boundary (CMB) (Williams and Garnero, 1996). The BMO, the initial thickness of which could have been 1000 km, slowly cooled down while vigorously convecting because of its high temperature and low viscosity. On a small scale, the process of solidification coupled with convective flow has been observed in lava lakes (Worster et al., 1993; Jellinek and Kerr, 2001) or ice lakes (Notz and Worster, 2006). However, suitable models capturing melting/solidification coupled with convective motions need to be developed.

Analytical works conducted in early years contain mainly mathematical solutions for one dimensional diffusion problems in an infinite or semi-infinite domain and for problems with simple initial and boundary conditions (Crank, 1984; Davis, 2001). More complex systems in terms of geometry or thermochemical parameters require numerical solutions. Including a transformation between solid and liquid phases presents a challenging numerical task since the position of the melting/freezing front is a part of the solution and so the moving boundary needs to be determined in space at each time.

A number of numerical methods for treating the moving boundary due to solidification or melting, and also being capable of handling convection in the melt, have been proposed (Crank,

* Corresponding author.
E-mail addresses: martina.ulvrova@ens-lyon.fr, mulvrova@gmail.com (M. Ulvrová).

0031-9201/$ - see front matter © 2012 Elsevier B.V. All rights reserved.
http://dx.doi.org/10.1016/j.pepi.2012.06.008

1984, and reference therein). These can be divided into two main groups: moving mesh front tracking methods and fixed grid numerical techniques. The former group solves different governing equations in each of the phases and latent heat effects enter via the heat balance boundary condition at the melting/freezing front. The latter group uses a static mesh and the same differential equations are applied in both phases. The position of the phase interface is then recovered from the temperature solution and the phase diagram.

The goal of this paper is to propose, implement and critically test suitable numerical tools for simulating a solidifying/melting system whose dynamics is closely coupled with convection in the melt. We start from two different codes that solve motion in a fluid: the finite element open source code Elmer (CSC – IT Center for Science, 2010), in which we use the formulation for a moving grid method, and the finite volume code StagYY (Tackley, 1993, 1996, 2008), in which we implemented the dynamic treatment of melting/solidification on a fixed grid.

These numerical tools are subsequently applied to benchmark test cases. We present a detailed comparison of heat flow, phase change front tracking and the nature of convection. The applicability of the different approaches is carefully analyzed and discussed.

In addition, we present a qualitative comparison of the three-dimensional numerical results with experimental work of Davis et al. (1984).

Finally, we focus on the thermal evolution of the magma ocean solidifying in the deep mantle during early Earth's history. We derive scaling relations for the heat transfer and apply these scalings to the BMO.

2. Physical model

In this section we describe the physics of a pure substance undergoing a crystallization/melting phase change. A Newtonian incompressible liquid in a domain $\Omega \in \mathbb{R}^2$ changes phase at a fixed temperature T_M. In the molten region, density differences due to temperature gradients induce convection through a buoyancy force term.

The basic set of conservation equations for mass and momentum in the Boussinesq approximation holds in the liquid:

$$\nabla \cdot \boldsymbol{v} = 0, \tag{1}$$

$$\frac{1}{\mathrm{Pr}}\frac{\mathrm{D}\boldsymbol{v}}{\mathrm{D}t} = -\nabla p + \nabla \cdot \left(\eta\left(\nabla \boldsymbol{v} + (\nabla \boldsymbol{v})^{\mathrm{T}}\right)\right) + \mathrm{Ra}\, T \boldsymbol{e}_z, \tag{2}$$

written in a dimensionless form. Length is scaled by the vertical thickness of the whole domain L, velocity vector $\boldsymbol{v}$ by κ/L, with κ the thermal diffusivity, time t by the diffusion time L^2/κ and pressure p by $\kappa\eta_L/L^2$ with η_L the dynamic viscosity of the liquid. $\boldsymbol{e}_z$ is a unit vector along a vertical direction pointing upward and η the dimensionless viscosity scaled by η_L. The solid is considered to be a non deformable medium with zero velocity everywhere.

The definition of the total time derivative $\frac{\mathrm{D}\bullet}{\mathrm{D}t}$ depends on the chosen reference frame. For the Eulerian description of motion $\frac{\mathrm{D}\bullet}{\mathrm{D}t} = \frac{\partial \bullet}{\partial t} + (\boldsymbol{v}\nabla)\bullet$, which reduces to $\frac{\mathrm{D}\bullet}{\mathrm{D}t} = \frac{\mathrm{d}\bullet}{\mathrm{d}t}$ when using the Lagrangian description of motion.

There are two dimensionless numbers appearing from the normalization of the conservation equations. The first one is the Prandtl number Pr, which is the ratio between momentum diffusion and thermal diffusion,

$$\mathrm{Pr} = \frac{\eta_L}{\rho_0 \kappa}, \tag{3}$$

where ρ_0 is the density at the temperature of the coldest wall. The second is the Rayleigh number, which relates the driving forces to the resistive mechanisms,

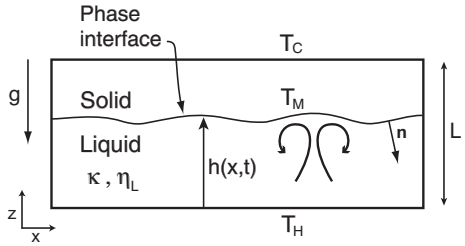

Fig. 1. Schematic picture of a convecting liquid layer that solidifies/melts. The layer is heated from below and cooled from above so that the upper part is frozen and the phase transformation remains in the computing domain.

$$\mathrm{Ra} = \frac{g\alpha L^3 \rho_0 \Delta T_t}{\kappa \eta_L}, \tag{4}$$

where g is the gravitational acceleration and α is the thermal expansion coefficient. $\Delta T_t = T'_C - T'_H$ is the total super-isentropic temperature difference between the hot ($T' = T'_H$) and the cold ($T' = T'_C$) boundaries (prime denotes physical dimension).

The third governing equation applying to liquid and solid, energy conservation without any volumetric heat source, is written as

$$\frac{\mathrm{D}T}{\mathrm{D}t} = \nabla^2 T. \tag{5}$$

The temperature field T is scaled as $T = (T' - T'_C)/(T'_H - T'_C)$. Normalized temperature T is thus bounded by 0 and 1 in the computational cavity.

Thermodynamical properties (thermal diffusivity κ, heat capacity at constant pressure C_P, thermal conductivity k) are considered to be constant and independent of temperature, and are the same for the liquid and solid. Density is also taken to be constant and the same for both phases following the Boussinesq approximation (density variations due to temperature gradients are only considered in the buoyancy term).

At the phase change interface, the following conditions must be verified. There are three requirements on temperature: continuity of temperature that is equal to the melting temperature, $[T]^+_- = 0$, and $T = T_M$, and a jump in the heat flux corresponding to the release or consumption of latent heat $\mathscr{L}$ (Crank, 1984; Davis, 2001),

$$[\nabla T \cdot \boldsymbol{n}]^+_- = \mathrm{St}\, \boldsymbol{u} \cdot \boldsymbol{n}. \tag{6}$$

The brackets $[\,]^+_-$ indicate the jump of a given quantity over the phase interface. $\boldsymbol{u} = (u_x, u_z)$ is the velocity of the phase change boundary and $\boldsymbol{n} = (n_x, n_z)$ its unit normal vector pointing toward the liquid, cf. Fig. 1. The Stefan number St is

$$\mathrm{St} = \frac{\mathscr{L}}{C_P \Delta T_t}. \tag{7}$$

It compares the latent heat to the specific heat C_P. The larger St, the more important latent heat effects are and thus the slower the interface moves.

In terms of velocity constraints, the melting front is a no-slip boundary, i.e. for a unit tangent vector $\boldsymbol{t}$, the condition $\boldsymbol{v} \cdot \boldsymbol{t} = 0$ must be fulfilled. The next condition results from mass balance allowing the density change over the phase transition. Suppose that the geometry of the solidifying system is as in Fig. 1, with the position of the interface described by the function $z = h(x,t)$. Then the vertical velocity of the interface, u_z, must satisfy (Davis, 2001)

$$\Delta\rho\, u_z = \rho_L\left(v_z - v_x \frac{\partial h}{\partial x}\right), \tag{8}$$

where $\Delta\rho$ is the difference between the densities of solid and liquid, $\Delta\rho = \rho_S - \rho_L$, and v_x and v_z are the horizontal and vertical

components of the fluid velocity vector $\boldsymbol{v} = (v_x, v_z)$. In our case $\Delta\rho = 0$, thus the above two conditions are satisfied if and only if $\boldsymbol{v} = \boldsymbol{0}$ at the melting front.

3. Front tracking method

The first numerical approach for the solidification/melting process with fluid flow in the melt involves treating the solid and the liquid as distinct domains coupled by the boundary conditions at the phase change front. At each time the position of the boundary is explicitly computed. In order to account for its motion, either mesh deformation or a suitable mapping that transforms the problem on a fixed mesh is required. This strategy is suitable for the isothermal phase change of a pure substance and might not be accurate enough when the state transformation happens over a finite temperature interval. Solving for proper equations, Eqs. (1), (2) and (5), involves finding the velocity field in the liquid and the temperature field in the solid and the liquid. As a part of the solution, the position of the melting/freezing front arises as it is not known a priori.

The finite element (FE) free software Elmer (CSC – IT Center for Science, 2010) is used to numerically solve the equations described above. First, the energy equation is solved using the velocity field from the previous timestep to give the new temperature distribution. Next, the Navier–Stokes equation is solved in order to determine the new velocity. The temperature field explicitly defines the new position of the melting/freezing front and the mesh nodes must be redistributed so as to follow the interface movement. The solution of the problem thus involves four steps, four particular solvers, that are weakly coupled. The linear systems related to different physical phenomena are solved one-by-one (using iterative or direct methods, cf. below) without any common iterations.

3.1. Navier–Stokes and heat equations

The classical Galerkin method (e.g. Hughes, 1987) implemented for simulations of natural convection often results in spurious oscillations whose origin is in the advection terms. Thus, several stabilization methods have been developed to overcome this problem including the residual free bubbles method (Baiocchi et al., 1993) or using Taylor–Hood elements (Taylor and Hood, 1973). In our simulations the stabilization scheme proposed by Franca et al. (1992) and Franca and Frey (1992) is applied.

The Galerkin discretization of partial differential equations by the finite element method (FEM) is applied with subsequent linearization of the nonlinear convective term in the Navier–Stokes equation. The Picard linearization used is somewhat slower in convergence than the Newton's method, but has a larger radius of convergence.

Two main strategies in searching for the solution of the linear set of discretized equations include direct and iterative methods. For small systems, it is desirable to use the former strategy, which finds the exact solution up to machine precision but demands a large memory usage. As a direct solver we use Unsymmetric MultiFrontal method (UMFPACK) (Davis, 2004). On the other hand, iterative solvers generate an improving approximate solution to the given problem. These are useful for 3D geometries or large 2D systems. As an iterative solver strategy, the BiConjugate Gradient Stabilised method (BiCGStab) (Van der Vorst, 1992) with incomplete LU (ILU) factorization as a preconditionner is used.

For the time-stepping strategy, the Crank–Nicolson scheme (Crank and Nicolson, 1947) is chosen. In a single time step, the coupling between individual solvers proceeds in a weak manner (computation of one step after another), thus no coupled iterations of the system are run.

3.2. Motion of the phase interface and mesh update

Eq. (6), which expresses the heat balance at the melting front, is used to obtain the velocity of the interface. Supposing that the interface moves only in the vertical direction z, its velocity in the z-direction u_z is obtained as

$$[\nabla T \cdot \boldsymbol{n}]_-^+ = \mathrm{St}\, n_z \left(u_z - D_u \nabla^2 u_z\right), \tag{9}$$

where an artificial diffusion D_u has been added because otherwise the algorithm is subject to numerical oscillations. In order not to significantly influence the results, the condition $D_u \ll \Delta^2$ for the diffusion factor must be fulfilled, with Δ being the characteristic grid size.

In order to compute the nodal heat fluxes in Eq. (9) for the solid and the liquid, respectively, the residual of the discrete system for the heat equation without the effects of boundary conditions is used. This procedure provides the most accurate estimate of the nodal fluxes.

The new position of the phase interface is then obtained from the computation of its motion within one time step $\Delta t : \delta h = u_z \Delta t$. In order to account for the movement of the melting front, which is always described by the same mesh nodes, the grid must be distorted. The new node distribution results from solving a non-physical elastic equation for the mesh displacement $\boldsymbol{d}$

$$-\nabla \cdot \left(\mu\left(\nabla \boldsymbol{d} + (\nabla \boldsymbol{d})^T\right) + \lambda \nabla \cdot \boldsymbol{d} I\right) = 0, \tag{10}$$

where I is the unity tensor. Fictive Lamé parameters μ and λ, representing the elastic properties of the mesh, are chosen arbitrarily and can eventually help to enhance the quality of the new mesh. We can express the Lamé coefficients in terms of Youngs modulus Y and Poisson ratio ν

$$\mu = \frac{Y\nu}{(1-\nu)(1-2\nu)}, \quad \lambda = \frac{Y}{2(1+\nu)}. \tag{11}$$

The larger the value of Y, the stiffer the mesh is. This might be particularly useful for adding local rigidity near singularities, i.e. around the corners. The larger the Poisson ratio, the better the elements maintain their volume until reaching the critical value of $\nu = 0.5$, when Eq. (11) becomes singular. Nevertheless, with smooth meshes these have only minor effects and we keep them constant for all numerical experiments.

Coupling between the distorted mesh and interface position comes through the Dirichlet boundary condition at the melting front where for the vertical displacement d_z the relationship $d_z = \delta h$ holds.

Using the displacement of nodes allows us to significantly reduce the computational time compared to completely regenerating the mesh at each time step. On the other hand, there is no way to ensure that the new mesh guarantees good computational precision since elements can be strongly strained. Thus, small changes in geometry are favorable for retaining a numerically accurate mesh.

Since movement of the mesh is involved, in Eqs. (1) and (5) the mesh velocity $\boldsymbol{v}_m$ must be accounted for. The so-called Arbitrary Lagrangian–Eulerian (ALE) description (Donea et al., 2004), in which the mesh nodes can be moved about an arbitrary distance in between nodes following the continuum movement (Lagrangian description) or being held fixed (Eulerian approach), is implemented. The total time derivative term is then

$$\frac{\mathrm{D}\bullet}{\mathrm{D}t} = \frac{\partial \bullet}{\partial t} + (\boldsymbol{c} \cdot \nabla)\bullet, \tag{12}$$

where $\boldsymbol{c}$ is the convective velocity, $\boldsymbol{c} = \boldsymbol{v} - \boldsymbol{v}_m$. In the Lagrangian approach, the mesh velocity is equal to the material velocity, i.e. $\boldsymbol{c} = \boldsymbol{0}$.

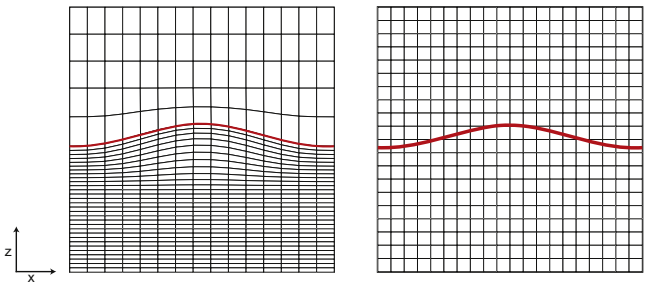

(a) Distorted mesh (b) Fixed grid mesh

Fig. 2. Schematic pictures of moving and non-moving mesh for single component Stefan problem in configuration depicted in Fig. 1. The melting front is denoted by the solid red line. (For interpretation of the references to colour in this figure legend, the reader is referred to the web version of this article.)

The Eulerian formulation keeps the mesh non-deformed, and thus $\boldsymbol{c} = \boldsymbol{v}$ holds. In the present model, the mesh motion is computed such that the phase change interface coincides with a mesh line.

3.3. Mesh

In 2D simulations quadrilateral bilinear elements are used. At the beginning of the computation, the grid is composed of rectangular elements that deform with the motion of the melting front. A schematic example of a deformed mesh is depicted in Fig. 2a with finer and coarser resolution in the liquid and solid, respectively. The red line represents the phase change front.

Input files for `Elmer` simulations together with mesh files corresponding to the simulations presented can be found at `http://perso.ens-lyon.fr/stephane.labrosse/Ulvrova_etal2012`. These can be also find in online supplementary material, cf. Appendix A.

4. Fixed grid method

In order to eliminate the necessity of explicitly satisfying the thermal conditions between the two phases, we can describe heat transfer in the solid and the liquid using a single governing equation for energy conservation written in terms of the enthalpy variable H on a fixed grid in an Eulerian reference frame (Crank, 1984). The system of Eqs. (5) and (6) comprising additionally the heat balance at the melting/freezing interface is replaced by a single equation

$$\frac{\partial H}{\partial t} + \boldsymbol{v} \cdot \nabla H = \nabla^2 T, \tag{13}$$

implicitly containing the effect of the phase change. The total enthalpy of the system is equal to the temperature in the solid part and is increased in the liquid part by the contribution from latent heat

$$H(T) = \begin{cases} T & \text{if} \quad T \leqslant T_{\mathrm{M}}, \\ T + \mathrm{St} & \text{if} \quad T > T_{\mathrm{M}}. \end{cases} \tag{14}$$

Conditions (14) can be combined into one single equation $H = T + \mathrm{St} f_{\mathrm{L}}$, with f_{L} the liquid fraction. Introducing the definition of enthalpy into Eq. (13) we obtain

$$c^{\mathrm{A}} \frac{\mathrm{D}T}{\mathrm{D}t} = \nabla^2 T, \tag{15}$$

with the nondimensional apparent heat capacity

$$c^{\mathrm{A}} = \frac{\mathrm{d}H}{\mathrm{d}T} = 1 + \mathrm{St} \frac{\partial f_{\mathrm{L}}}{\partial T}. \tag{16}$$

In this case, a temperature field is obtained as a solution, which is used to reconstruct a posteriori the position of the melting/freezing front. However, the mechanical boundary condition, which requires the solid not to deform, must also be fulfilled. This is achieved by imposing a viscosity strongly dependent on the liquid fraction f_{L}. Here, we use

$$\eta = \exp\left(B(1 - f_{\mathrm{L}})\right), \tag{17}$$

where B is a parameter that defines the viscosity ratio between the solid and the liquid. Equations for fluid flow, Eqs. (1) and (2), are then solved in the whole cavity.

Taking f_{L} as the Heaviside step function implicitly imposes the condition Eq. (9) at the solid liquid boundary. It leads to a discontinuity in the enthalpy. However, treating singularities with methods that compute derivatives using finite differences requires regularization techniques. Hence, when using the enthalpy formulation the phase change is not sharp but always happens over a mushy region of finite thickness. Thus, the enthalpy method is naturally suitable for melting/solidification processes of solids/liquids consisting of multiple components.

Several numerical approaches have been developed to solve Eq. (13) including source update methods, where the latent heat effects are put into a separate term corresponding to the source term, enthalpy linearization or using the apparent heat capacity (e.g. Voller, 1985, 1996; Voller et al., 1990). In our paper we choose the latter one, thus solving governing Eq. (15) instead of Eq. (13) together with the mass and momentum equations. The advantage is that the energy equation remains formally the same as for the standard heat transfer model and only the definition of the heat capacity changes, which enables the phase change to be easily incorporated into an already existing convection code. On the other hand, the drawback of using a temperature dependent heat capacity c^{A} is that it forbids writing Eq. (15) in a fully conservative finite volume form. Thus, this method is more suitable for small Stefan numbers, roughly lower that 1, for which the temperature dependence of c^{A} is limited. As a remedy for high Stefan number cases, fine spatial resolution can be employed to ensure a balanced heat budget at steady state. A fine resolution is also needed in the vicinity of the phase boundary where the largest enthalpy gradient occurs.

In order to model a phase change using an effective heat capacity we have to define the liquid fraction as a function of temperature. For a sharp phase transformation this should be a step function with value one in the liquid and zero in the solid. As mentioned earlier, smoothing of the discontinuity must be incorporated in order for the system to be solved numerically. Hence, the phase change occurs over a temperature interval 2ϵ that defines the width of a mushy region and we choose the phase fraction function to be

$$f_{\mathrm{L}} = \frac{1}{2}\left(1 - \tanh\left(\frac{T_{\mathrm{M}} - T}{\epsilon}\right)\right), \tag{18}$$

which gives us the derivative needed in Eq. (15). The parameter ϵ can be seen as a physical parameter linked to the width of the mushy region, which is observed to exist in experiments of phase changes in complex compounds. The extent of the mush also depends on the vigor of convection that determines the temperature gradients at the phase change interface.

The f_{L} function together with viscosity η are depicted in Fig. 3. The critical parameters in these definitions are the temperature phase interval 2ϵ and the parameter B that controls the viscosity values in the solid and mushy regions.

The physical situation that we consider here is different from that of solid–solid phase transitions in the Earth's mantle, where an effective heat capacity is introduced to treat latent heat effects

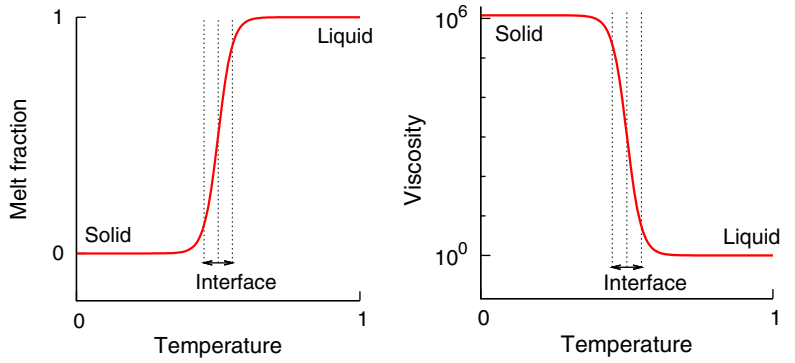

(a) Liquid fraction as a function of temperature. (b) Viscosity as a function of temperature.

Fig. 3. Melt fraction and viscosity as a function of temperature for the enthalpy method. Dashed vertical lines denote the interval of phase transformation, in this case being 10% of the total temperature range ($\epsilon = 0.05$).

due to a solid–solid phase transition in mantle convection simulations (Christensen and Yuen, 1985): firstly, the dynamics associated with solid–solid phase transformations in the interior of the Earth are dominated by changes in their depth (pressure) caused by lateral temperature variations, which contrasts to melting that we here consider to be purely dependent on temperature; also, with a solid–solid phase change in the mantle, flow is allowed across the boundary which differs from our case where the solid does not deform.

We implement the liquid/solid transition into the finite volume code StagYY; cf. Tackley (1993, 1996, 2002, 2008) for technical details of the code, and repeat here only some of its important technical aspects.

StagYY is intended to model Rayleigh–Bénard convection of extremely viscous fluids in the infinite Prandtl number approximation, so the time derivative in Eq. (2) is neglected. A staggered grid discretization is used, hence velocity components are defined at cell boundaries while pressure and temperature are defined at cell centers. Of great importance is that StagYY is capable of handling large viscosity variations of up to 19 orders of magnitude (Tackley, 2008).

Viscosity, which is also defined in the cell center, needs to be interpolated to the cell corners (in 2-D) or cell edges (in 3-D) in order to compute the viscous shear stresses. There are several viscosity averaging strategies including harmonic mean, arithmetic mean or geometric mean. The choice of the averaging law is particularly important in regions of abrupt viscosity change (Deubelbeiss and Kaus, 2008), i.e. in this case around the phase transition. Arithmetic averaging would give a stiffer mush while harmonic averaging would allow the mush to deform more (Schmeling et al., 2008). These differences would be noticeable only in cases where insufficient spatial resolution is employed. Geometric averaging lies in the middle of arithmetic and harmonic mean and we decide to use this for all of our experiments.

The governing Eq. (15) of the enthalpy formulation of the Stefan problem is discretized on a regular non-deforming mesh and treated using the Eulerian description of motion. The position of the melting front is then read off the temperature solution. A schematic example of the grid together with the phase boundary is depicted in Fig. 2b.

5. Benchmarking both codes

In order to test our numerical solutions we performed two- and three-dimensional calculations in several different settings. Firstly, we test our tools using an exercise proposed by Bertrand et al. (1999) in which a 2D solid cavity is heated from a vertical wall so that the single component phase subsequently melts.

Secondly, we compare the two methodologies for solving the phase change problem coupled with Rayleigh–Bénard convection in the melt. The liquid layer is heated from below and cooled from above so that the melting front stays in between.

Next, we draw a qualitative comparison between our 3D numerical calculations and experimental results published in Davis et al. (1984) for a horizontal layer heated from below.

Finally, we quantify the effects of the two parameters needed when employing the enthalpy formulation: the temperature interval 2ϵ over which the phase transition occurs and the parameter B defining the viscosity ratio between the solid and the liquid.

5.1. Melting driven by natural convection in a square cavity

Consider a square cavity that is initially solid and maintained at an initial temperature that is equal to the melting temperature $T_M = 0$. Insulating horizontal walls are imposed and the right vertical wall is kept at T_M, cf. Fig. 4. Zero velocity initial conditions are prescribed and all boundaries are no-slip.

At time $t = 0$ the temperature of the left vertical wall is raised and kept at a temperature $T_H > T_M$, in order to allow melting to start. After the initial transient stage dominated by heat conduction, convection in the melt arises as the thickness of the liquid layer increases. Finally, heat transfer through the liquid phase is controlled by convection. The phase change interface remains planar when heat transfer occurs by conduction. As early as convection sets up, the upper part of the cavity melts at a higher rate due to high temperature gradients.

Numerical experiments are first performed using the `Elmer` code. As was described in Section 3, the position of the melting/

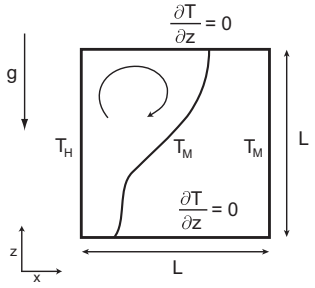

Fig. 4. Schematic view of the test case after Bertrand et al. (1999). The enclosure is heated from the left vertical wall, which causes a progressive melting. After an initial state of pure conduction, natural convection occurs in the liquid and results in more extensive melting in the upper part of the cavity. Horizontal walls are kept insulated and the right vertical wall is maintained at the melting temperature T_M.

freezing front is always assigned to the same mesh nodes, resulting in deformation of the grid corresponding to latent heat consumption/release. Consequently, the number of mesh nodes changes neither in the solid nor in the liquid during a simulation. Thus, for all numerical experiments, both the solid and the liquid must exist from the beginning to the end of the run. Hence, in the set-up test case we use as initial conditions for the temperature the analytical solution of the 1D Stefan problem (Davis, 2001) resulting after time $t = 5 \times 10^{-3}$ has elapsed. The parameter values of the simulation correspond to Case 3 in Bertrand et al. (1999), i.e. $\mathrm{Pr} = 50, \mathrm{Ra} = 10^7$ and $\mathrm{St} = 10$. The initial position of the phase front is thus $x_{\mathrm{init}} = 0.031115$.

The rectangular 2D mesh is composed of bilinear elements. Initial equal spacing in both directions is imposed. We use 60 elements in the vertical direction and 15 and 35 elements in the horizontal direction in the liquid and solid parts of the cavity, respectively. A fixed time step $\mathrm{d}t = 2 \times 10^{-5}$ is used in the Crank–Nicolson method.

Snapshots of the temperature field at four different times are depicted in Fig. 5. A comparison of our solution with the synthesis of results published in Gobin and Le (2000) is plotted in Fig. 7. Fig. 7a shows the time evolution of the average Nusselt number, which is the dimensionless heat flux density, over the hot vertical wall. Fig. 7b shows the position of the melting front at time $t = 0.1$.

Numerical results published in Gobin and Le (2000) show a large dispersion of possible solutions, e.g. in the case of melting front positions at time $t = 0.1$ (Fig. 7b) the dispersion at $z = 1$ is around 9%. The differences are caused by the various implementations of the time and spatial resolutions and not by the mathematical formulations used (Gobin and Le, 2000). However, in the absence of an exact solution, it is hard to know which code produces the most accurate solution.

Nevertheless, our solutions lie in the region of published solutions, being closest to the results of Le Quéré or Wintruff (Gobin and Le, 2000). The model of Le Quéré uses the enthalpy formulation. The enthalpy is approximated in this case by a continuous and piecewise linear function with phase change interval 0.001. A 2nd order centred finite volume discretization is used in the spatial domain. Wintruff uses the control volume finite element approach together with a front tracking method to account for the latent heat effects; the interface position is thus calculated explicitly.

From this benchmark comparison we conclude that Elmer provides an accurate tool capable of handling the crystallization/melting processes closely coupled with convective motions in the liquid. The impossibility of modelling complete solidification/melting of the cavity is compensated by the small computational cost.

The same exercise was repeated with the StagYY code, which allows the computation of the phase transformation and convective motion in the infinite Prandtl number approximation. It is important to note that the formulation we have chosen is not suitable for this test. As all the solid is initially held at the solidification temperature, the last term in Eq. (16), which should be non-zero only in the mushy region between the solid and the liquid, contributes to the solution over the whole solid. We thus modify the phase fraction function so that the mushy region occurs mainly in the liquid by adding a shift ϵ_{S}

$$f_{\mathrm{L}} = \frac{1}{2}\left(1 - \tanh\left(\frac{T_{\mathrm{M}} + \epsilon_{\mathrm{S}} - T}{\epsilon}\right)\right), \tag{19}$$

and we use $\epsilon_{\mathrm{S}} = \epsilon$.

The computations were performed on a mesh with 256×256 finite volumes. The same initial conditions described above for Elmer were used.

Snapshots of the temperature field are shown in Fig. 6. Comparison of the interface position at time $t = 0.1$, which is in this case represented by the isotherm with the temperature value $T = T_{\mathrm{M}} + \epsilon_{\mathrm{S}}$, together with time evolution of the heat flux over the hot vertical wall, are presented in Fig. 7. While the form of the phase interface falls into the interval of solutions obtained in Gobin and Le (2000), the most significant difference is observed in the time dependence of the Nusselt number. This difference is not caused by neglecting the inertia force but rather is related to the limitation of the method implemented.

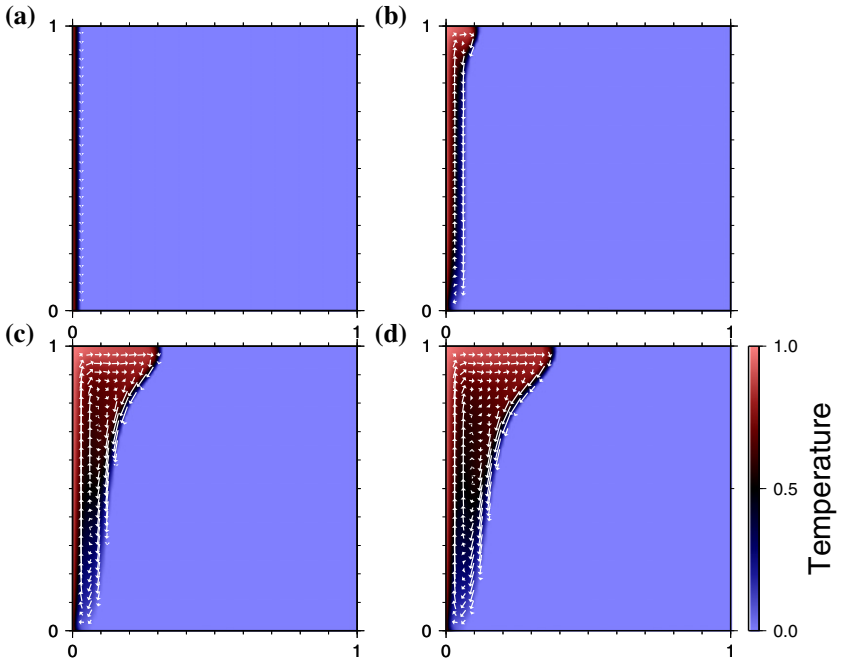

Fig. 5. Snapshots of temperature (color scale) and velocity field (vectors) at times (a) $t = 0.005$ (b) $t = 0.03$ (c) $t = 0.08$ (d) $t = 0.1$. In an initially nearly completely solid cavity with temperature equal to the zero melting temperature ($T_{\mathrm{M}} = 0$), progressive melting occurs from the hot left vertical wall. (Case with $\mathrm{Pr} = 50, \mathrm{Ra} = 10^7, \mathrm{St} = 10$.) Results were obtained with the moving mesh grid code. (For interpretation of the references to color in this figure legend, the reader is referred to the web version of this article.)

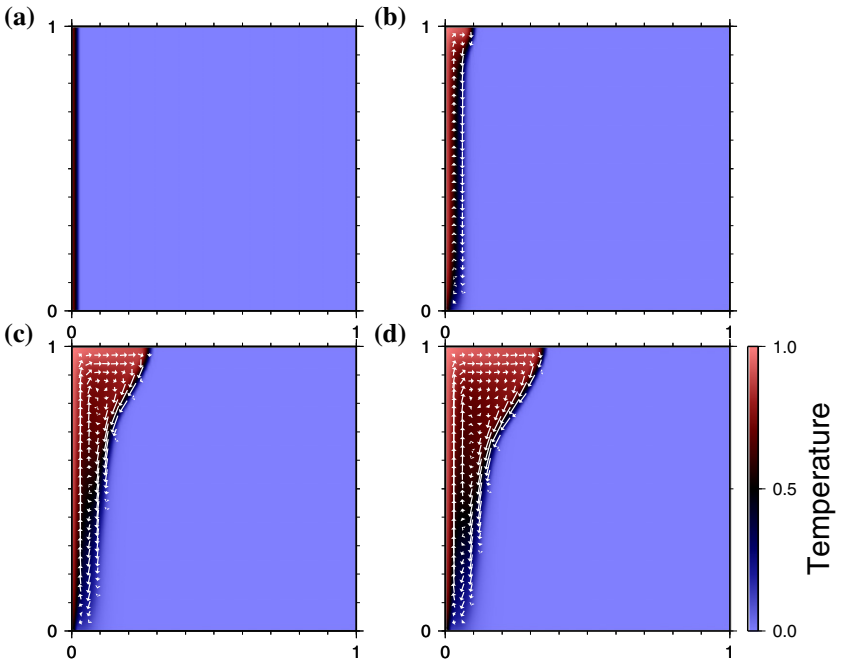

Fig. 6. The same caption as for Fig. 5, but the results were obtained with the fixed grid StagYY code and for Pr=∞.

5.2. Rayleigh–Bénard convection during melting of a single component solid

As a second test case, melting in a square cavity heated from below is studied. The schematic layout is depicted in Fig. 8. In a box of height L, we impose a temperature difference between the top and bottom boundaries: $T_C = 0$ at the upper surface and $T_H = 1$ at the lower one, so that with an imposed melting temperature of $T_M = 0.5$ the upper region stays solid while the lower one is molten. If the Rayleigh number is high enough, Rayleigh–Bénard convection establishes itself in the liquid, which leads to the development of corrugations of the phase change interface.

Vertical walls are taken to be insulating. All boundaries are considered to be no-slip and we start from a conductive solution, $T = 1 - z$, with perturbations $P = 0.1 \sin(\pi x) \sin(2\pi z)$ in the liquid layer. With $T_M = 0.5$, initially 50% of the computing volume is liquid. Parameters of the test case are chosen to be as follows: $St = 0.1$ and $Ra = 10^5$. As time increases the fluid starts to convect. Ascending current develops in the middle of the cavity and the fluid descends along the vertical walls. As a consequence, the initially flat interface becomes corrugated due to the variable temperature gradient normal to the melting front.

The two numerical implementations differ in treating the momentum equation. In the fixed grid method, an infinite Prandtl number approximation is considered. Based on laboratory experiments, it was shown by Krishnamurti (1970a,b), that this simplification is valid for $Pr > 100$. We thus use $Pr = 1000$ for the distorting grid method so as to make the comparison of the two sets of results meaningful.

In the moving mesh code, the mesh used during the simulation consists of 50 elements in horizontal direction and 40 and 10 elements in vertical direction in the liquid and the solid, respectively, with the chosen timestep size equal to 2×10^{-5}. The enthalpy method formulation is solved on a grid consisting of 128×256 elements. The timestep is chosen so that the Courant number does not exceed 1. A clear advantage of the moving grid method appears here: very few grid points can be used in the solid since only diffusion proceeds there. Thus it allows optimization of the computational cost. On the contrary, the enthalpy method must handle large viscosity contrasts in the vicinity of the phase transition and thus requires fine mesh resolution. As a possible strategy adaptive grid refinement can be employed (e.g. Davies et al., 2011), which allows having a fine mesh resolution where needed. However, its implementation is beyond the scope of this work, and we use a static regular mesh that is dense enough to manage the large viscosity variations.

Comparison of results from the two methods is shown in Figs. 9–13. Fig. 9 shows the time evolution of the mean temperature in the cavity and the average Nusselt number over the hot wall. At steady state, the relative difference between the two solutions is less than 1% for the mean temperature and around 2% for the bottom heat flux.

These differences also show up in the thermal profiles displayed in Fig. 10, where vertical temperature profiles are presented at four different times at a distance $x = 0.25$ from the left boundary. The convecting core is slightly colder with the moving mesh code than with the fixed grid one. Corresponding velocity profiles are plotted in Fig. 11. Convective velocities in the liquid are mildly faster for moving mesh simulations.

A comparison of the interface position obtained by the two approaches is depicted in Fig. 12. In the case of the distorted grid, larger amplitudes of corrugations are obtained. Comparing the position of the melting front at time $t = 0.2$, the relative difference between the two average solutions is 0.8%. The maximum of the difference between deviations of the interface positions is 0.006.

Snapshots of the complete temperature field at four different times using both methods together with maps of their difference are depicted in Fig. 13. All results show an excellent agreement in the temperature fields. The differences are concentrated around the transition between the two phases. Compared to the results of Viswanath and Jaluria (1993), the two sets of our solutions show much better agreement in terms of interface position and temperature structure. In the case of Viswanath and Jaluria (1993) the large discrepancies between the solutions might be caused mainly by the insufficient resolution they used within the enthalpy approach. In contrast to what Viswanath and Jaluria (1993) reported,

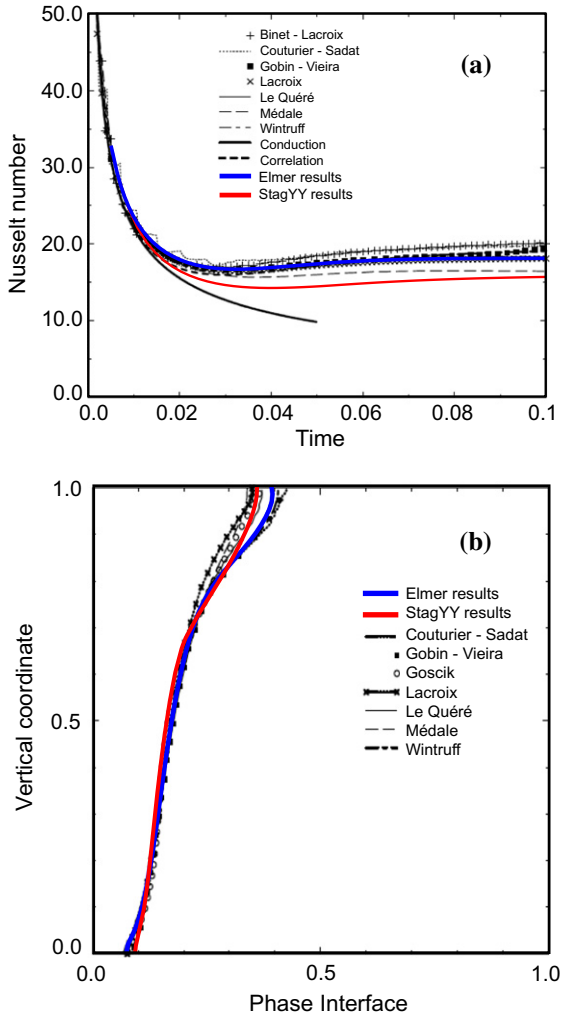

Fig. 7. Comparison of melting driven by natural convection test case with results published in Gobin and Le (2000). (Case with $\mathrm{Pr} = 50, \mathrm{Ra} = 10^7, \mathrm{St} = 10.$) (a) Time evolution of flux over the hot wall. (b) The interface position at time $t = 0.1$ (For interpretation of the references to colour in this figure legend, the reader is referred to the web version of this article.).

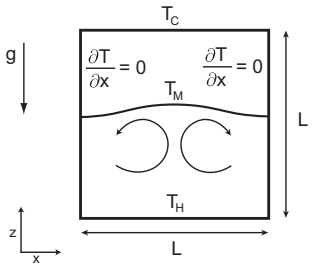

Fig. 8. Schematic picture of the set up for the second test case with solidification/melting of a liquid layer with developed Rayleigh–Bénard convection. The phase change front is maintained at a fixed temperature T_M whose value lies between the temperature of the bottom boundary T_H and upper boundary T_C. Vertical walls are insulating and no-slip boundary conditions are applied on all boundaries.

the interface positions obtained by the moving mesh method are always higher than those obtained by the enthalpy method.

5.3. Pattern selection in a crystallizing 3D convective horizontal layer

Davis et al. (1984) experimentally examined a single-component liquid that solidifies/melts in a plane layer heated from below

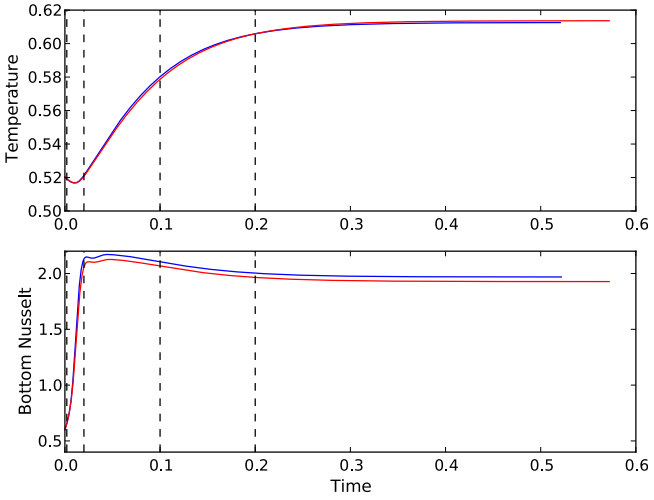

Fig. 9. Time evolution of the mean temperature in the cavity (upper figure) and mean Nusselt number over the hot bottom boundary (lower figure). Solid blue lines represent solutions obtained by the front distorted grid. Solid red lines result from the fixed grid enthalpy method. Vertical dashed lines indicate times when snapshots of Fig. 10–13 were taken. (Case with $\mathrm{Pr} = 1000$ (blue) and $\mathrm{Pr} = \infty$ (red), $\mathrm{Ra} = 10^5, \mathrm{St} = 0.1.$) (For interpretation of the references to colour in this figure legend, the reader is referred to the web version of this article.)

and cooled from above. The convective pattern established (rolls or hexagons) depends on the ratio of solid to liquid thicknesses A and the Rayleigh number. Davis et al. (1984) chose to relate all results to a purely conductive state in which the interface is planar. Thus, A is the ratio of the two heights in the case where only heat conduction proceeds. Small values of A lead to roll-like convective pattern selection whereas large A results in hexagonal convection.

Here, we qualitatively study these results and show the transition between these two configurations. Numerical simulations are carried out with the `StagYY` code, which is fully parallelized using domain decomposition and the Message Passing Interface library (MPI). We use a 3D layer with an aspect ratio of 8 in both horizontal directions, and $256 \times 256 \times 128$ grid cells in the two horizontal and vertical directions, respectively. Heating from below is imposed with insulating vertical walls and zero velocities at all boundaries. We pick the same parameters used in laboratory experiments, cf. Fig. 3a and b in Davis et al. (1984). Results of the first case, computed for $\mathrm{Ra} = 8.4 \times 10^3$ and $A = 0.03$, i.e. a liquid layer approximately thirty times thicker than the solid one for pure conduction, are presented in Fig. 14a. We show the corrugated solid–liquid interface at a state close to the steady state. Indeed, we observe convective roll patterns. A second experiment is performed for $\mathrm{Ra} = 1.1 \times 10^4$ and $A = 0.36$, i.e. the liquid layer approximately three times as thick as the solid. Results are shown in Fig. 14b. In this case, hexagonal patterns are observed, in agreement with the experimental observations of Davis et al. (1984).

5.4. Choice of parameters in the enthalpy method

In order to test the influence of the two numerical parameters appearing in the enthalpy method (temperature interval 2ϵ over which the phase transformation happens, and which is related to the width of the mushy two-phase region, and the viscosity contrast B between the solid and the liquid), we perform a series of experiments with the following set-up: fixed temperatures at the bottom ($T_H = 1$) and the top ($T_C = 0$) are imposed together with insulating vertical walls and zero shear stress on the bottom and vertical boundaries. The velocity condition at the top boundary must be no-slip to further prevent deformation of the solid. The

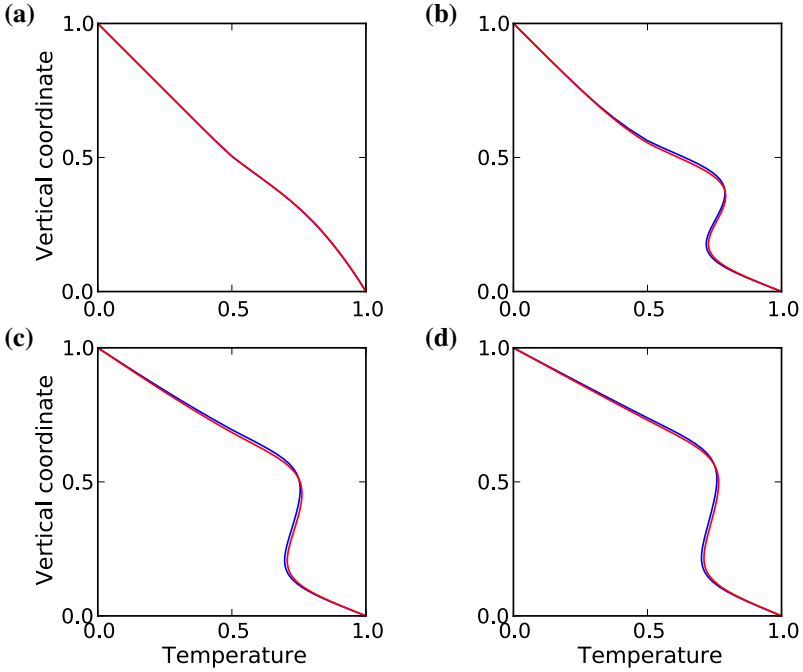

Fig. 10. Vertical profiles of horizontal temperature at $x = 0.25$ for four different times (a) $t = 0.002$ (b) $t = 0.02$ (c) $t = 0.1$ and (d) $t = 0.2$. Solid blue lines represent solutions obtained with the distorted grid code. Solid red lines result from the fixed grid enthalpy code. (Case with Pr = 1000 (blue) and Pr = ∞ (red), Ra = 10^5, St = 0.1.) (For interpretation of the references to colour in this figure legend, the reader is referred to the web version of this article.)

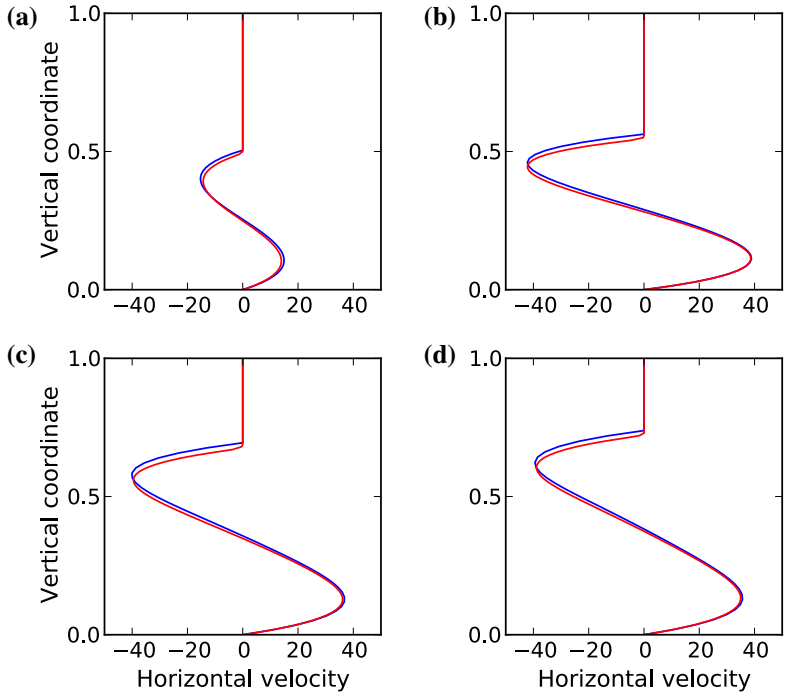

Fig. 11. Vertical profiles of horizontal velocity at $x = 0.25$ for four different times (a) $t = 0.002$ (b) $t = 0.02$ (c) $t = 0.1$ and (d) $t = 0.2$. Solid blue lines represent solutions obtained with the distorted grid code. Solid red lines result from the fixed grid enthalpy code. (Case with Pr = 1000 (blue) and Pr = ∞ (red), Ra = 10^5, St = 0.1.) (For interpretation of the references to colour in this figure legend, the reader is referred to the web version of this article.)

melting temperature is chosen to be $T_M = 0.5$, and Ra $= 3 \times 10^5$ and St $= 0.1$ are imposed. Steady convection in a square box is then computed on a 128×128 grid.

The temperature field, together with the viscosity for two different values of parameter B, are depicted in Fig. 15. The phase change temperature interval is here $\epsilon = 0.05$. Fig. 15e shows the difference between the two solutions with the highest discrepancies around the phase transformation. This is caused by the fact that the parameter B primarily affects the viscosity gradients in the mush that in turn controls velocity values in this transition. The higher the value of B the lower the velocities in the two-phase region due to higher viscosity gradients. In the limiting case,

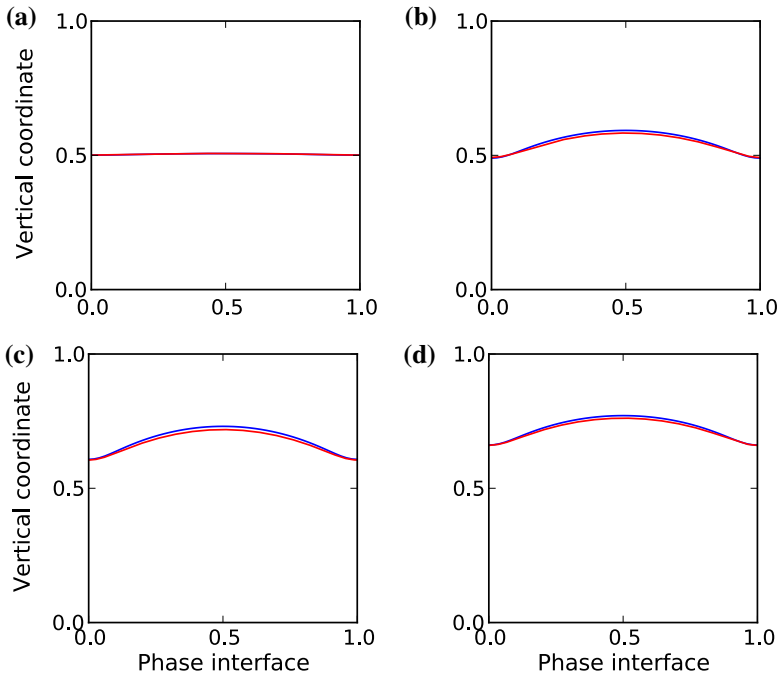

Fig. 12. Positions of the phase change interface at four different times (a) $t = 0.002$ (b) $t = 0.02$ (c) $t = 0.1$ and (d) $t = 0.2$. Solid blue lines represent solutions obtained with the distorted grid code. Solid red lines result from the fixed grid enthalpy code. (Case with Pr = 1000 (blue) and Pr = ∞ (red), Ra = 10^5, St = 0.1.) (For interpretation of the references to colour in this figure legend, the reader is referred to the web version of this article.)

velocities go to zero for temperatures higher than the melting temperature. However, having large viscosity gradients is numerically challenging. Thus, we determine the minimum value of B sufficient to create a stagnant solid region and being able to sufficiently reduce the velocity values in the mush, by running a systematic investigation. The effect of B is shown in Fig. 17a where we plot, as a function of B, the maximum of the relative difference between the temperature for the given value of B and that obtained for $B = 13$ (having a viscosity contrast of 2×10^{11}), chosen as a reference. The maximum relative difference can be kept below 10% if the viscosity contrast is larger than 10^3, which is the minimum to keep the solid from deforming. This is in agreement with experiments carried out for convection with strongly temperature dependent viscosity when a stagnant lid is formed for high enough viscosity ratios (Davaille and Jaupart, 1993).

The effect of the phase change interval ϵ is shown in Fig. 16 where two cases with $\epsilon = 0.005$ and $\epsilon = 0.05$ are compared (with $B = 6$ for both experiments, corresponding to a viscosity contrast of 2×10^5). Fig. 16a and b show the phase change interval in the two cases. The main effect of changing ϵ is to change the thickness of the two-phase region. This thickness ϵ_z can be related to ϵ by

$$\epsilon_z = \frac{\epsilon L}{\int_0^L \frac{\partial T}{\partial z}|_{\text{surf}} dx}. \tag{20}$$

As a normalization factor, the mean temperature gradient at the surface is suitable since it is approximately constant in the solid (Fig. 10).

Fig. 16e depicts the relative difference between the two temperature solutions. Again, the largest difference between solutions is found around the melting front. Results of the systematic study are displayed in Fig. 17b. As a reference solution, the case with the smallest $\epsilon = 0.001$ is taken. The relative difference is less than 1% for ϵ_z of order Δz or less and is kept below the 10% level for nearly the whole studied interval. Using a larger epsilon amounts to treating a large two-phase region and could be a good modelling approach for a convection situation in which a thick mushy layer develops.

6. Thermal evolution of the crystallizing basal magma ocean (BMO)

In this section we use the tools developed above to conduct a series of numerical experiments to derive the heat transfer laws for the convecting liquid layer undergoing crystallization/melting. These laws are subsequently applied to the magma ocean that could have been lying between the Earth's core and solid mantle since the formation of the planet (Labrosse et al., 2007).

6.1. Heat transfer by Rayleigh–Bénard convection interacting with a freezing front

We consider the setting depicted in Fig. 1 where a liquid layer heated from below underlies the solid layer, similar to the second test case. The interface is locked in the computing box as we impose for the melting temperature $T_C < T_M < T_H$.

The dimensionless heat flux is expressed by the Nusselt number, here termed effective since it is written with variables applying to the liquid layer,

$$\text{Nu}_{\text{eff}} = \frac{Q}{\frac{k\Delta T_L}{\langle h \rangle}}, \tag{21}$$

where Q is the actual heat flux density coming in and out of the box, $\Delta T_L = T'_H - T'_M$ the temperature difference across the convective zone and $\langle h \rangle$ its average thickness. We want to describe Nu_{eff} as a function of the effective Rayleigh number based on the temperature difference ΔT_L and $\langle h \rangle$,

$$\text{Ra}_{\text{eff}} = \frac{g\alpha\langle h \rangle^3 \rho_0 \Delta T_L}{\kappa \eta_L}. \tag{22}$$

Combining with Eq. (4) we have $\text{Ra}_{\text{eff}} = \langle h \rangle^3 (1 - T_M)\text{Ra}$. Here, $\langle h \rangle$ does not have any physical dimension. For the sake of simplicity,

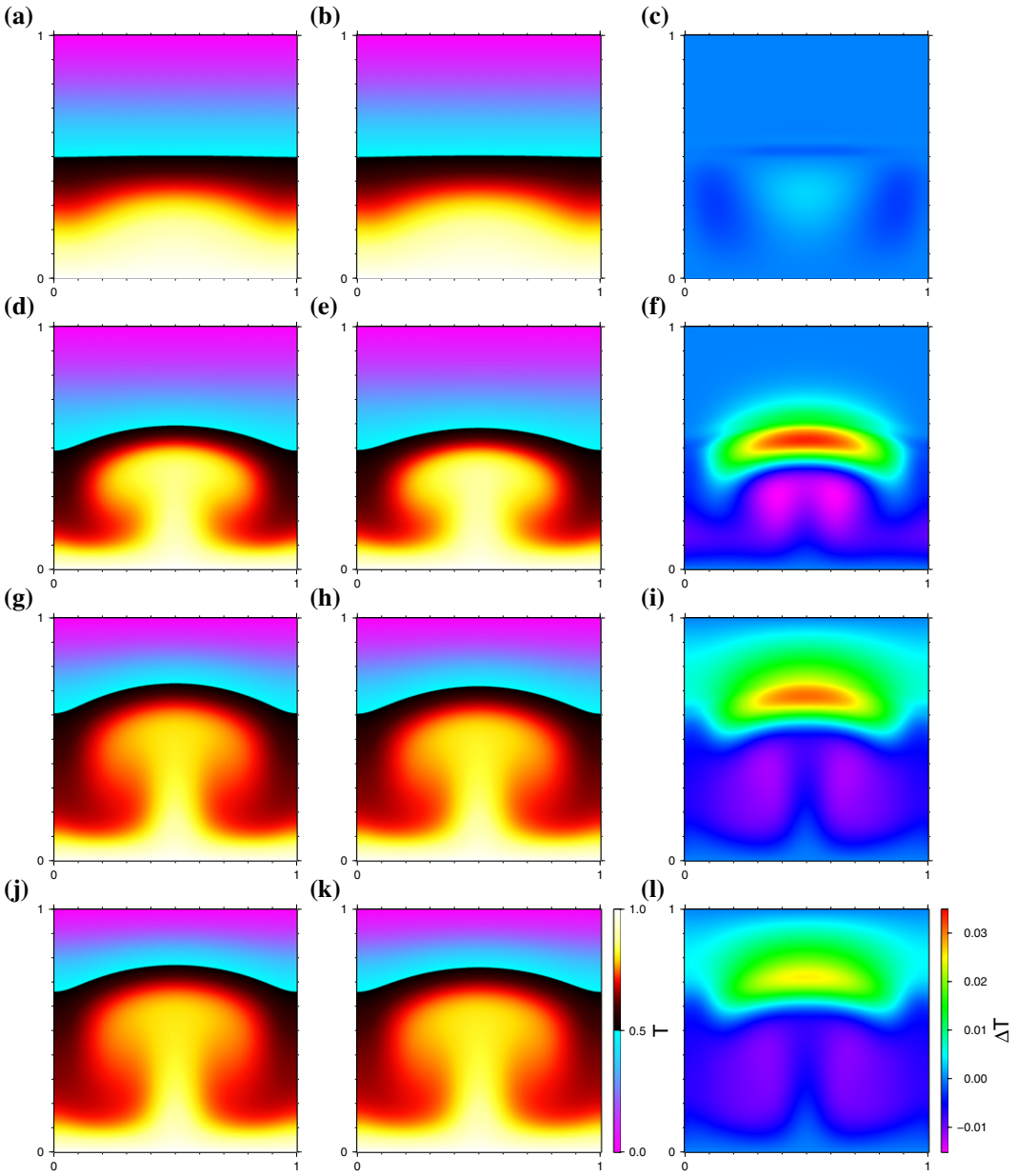

Fig. 13. Temperature field at four different times corresponding to Fig. 12 and dashed lines of Fig. 9. In the first column, solutions obtained with the moving mesh grid code are displayed. The second column depicts resulted obtained with the fixed grid enthalpy code. The third column shows the absolute difference between the two solutions at a given time. The melting temperature is $T_M = 0.5$. (Case with $\mathrm{Pr} = 1000$ (first column) and $\mathrm{Pr} = \infty$ (second column), $\mathrm{Ra} = 10^5, \mathrm{St} = 0.1$.)

we use the same symbol as above in Eq. (22). In the numerical experiments $\mathrm{Ra}_{\mathrm{eff}}$ is calculated a posteriori, Ra being imposed as an input parameter. We explore the $\mathrm{Nu}_{\mathrm{eff}}(\mathrm{Ra}_{\mathrm{eff}})$ relationship at two different Prandtl numbers, $\mathrm{Pr} = 7$ (equivalent to that of water) and $\mathrm{Pr} = \infty$. Clarification of the parameter choice is discussed below in Section 6.2 and is motivated by our intention to use the scaling laws for the BMO. We do not aim to simulate the long term cooling history of the system but focus on heat transfer at statistical steady-state. All experiments are thus conducted with a balanced energy budget.

Experiments at $\mathrm{Pr} = 7$ and $\mathrm{St} = 0.9$ are performed with the moving grid method. The aspect ratio of the computation domain is kept at a value of 4 but the resulting liquid layer has an aspect ratio in the range from 5 to 9. The number of finite elements in the grid depends on the value of the Rayleigh number. The finest resolution for the highest Rayleigh number contains 500 elements in the horizontal direction and 85 and 10 elements in the vertical direction in the solid and liquid, respectively. Most of the calculations are performed on a grid with 300 elements in the horizontal direction and 45 and 10 elements in the vertical direction in the liquid and solid, respectively. The grid is refined in the vertical direction in the thermal boundary layers in the liquid. The bottom and vertical velocity boundary conditions in the liquid are free slip. The vertial walls (in the solid and the liquid) are insulating. The initial condition for temperature is a linearly varying profile in the solid. In the liquid for cases with small Rayleigh numbers an isothermal interior is prescribed with boundary layers at top and bottom plus small random perturbations. The phase front is planar at the beginning of the run. Its initial position is fixed at a height of 0.6. Cases at high Rayleigh numbers were initiated from the final states of low Rayleigh number cases since the initial state has little effect on the final state for these runs.

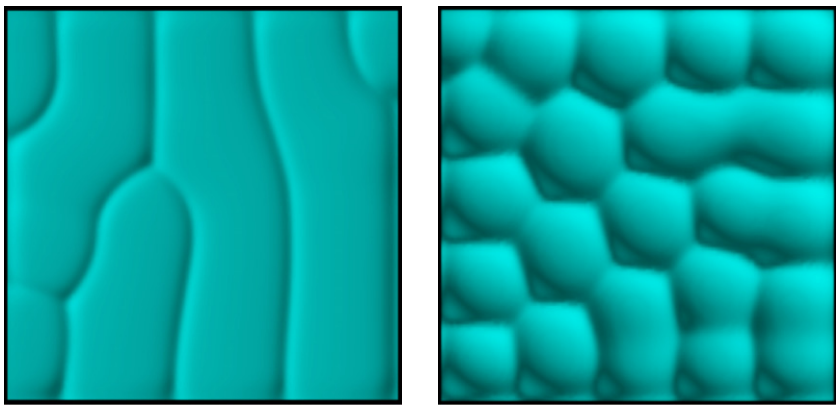

(a) Roll-like patterns. (b) Hexagonal patterns.

Fig. 14. 3D corrugated phase change interface in two different configurations corresponding to the results of Davis et al. (1984) Fig. 3a and c, depicting the roll and hexagonal planforms, respectively. Computed with the StagYY code in a cavity with an aspect ratio of 8 in both horizontal directions for St = 1 and (a) Ra = 8.4×10^3 (b) Ra = 1.1×10^4.

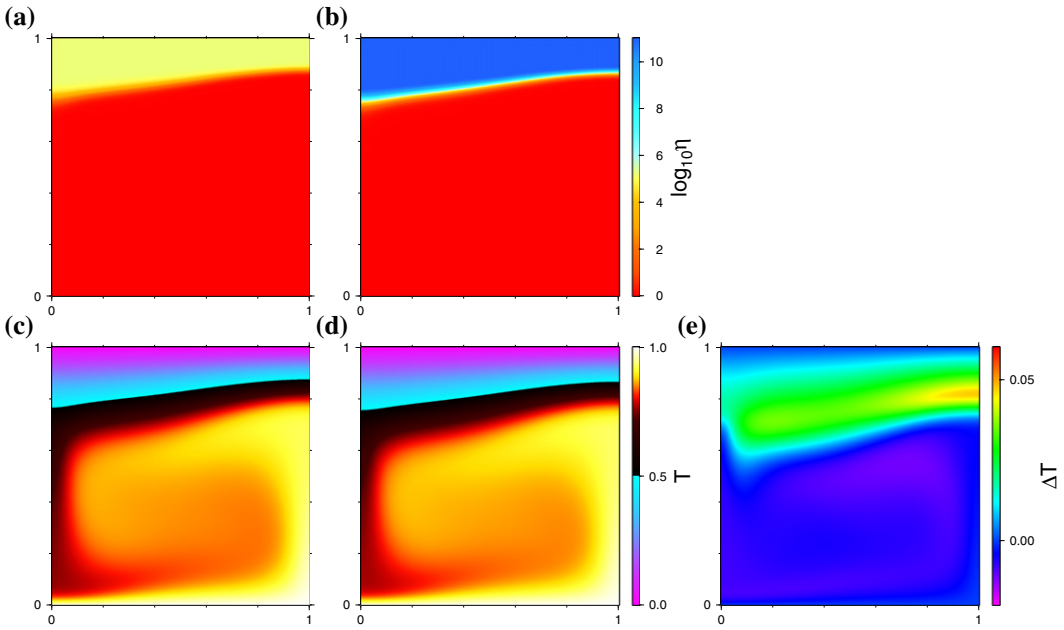

Fig. 15. Influence of the viscosity contrast between the solid and the liquid in the fixed grid code. Viscosity field (a) $B = 6$ (b) $B = 13$ and (c)–(d) corresponding temperature fields at steady state. (e) difference between the two temperature solutions. (Case with $\mathrm{Pr} = \infty, \mathrm{Ra} = 3 \times 10^5, \mathrm{St} = 0.1$.)

Experiments at infinite Prandtl number where inertia is neglected and St = 0.1 are done using the enthalpy method implemented in StagYY. We changed St because, for a given spatial resolution, a lower St ensures better energy conservation in the system. We compared calculations with both values using StagYY and found no significant effect on the dynamics of the flow and heat characteristics as both Stefan numbers are low enough.

We run experiments at aspect ratios of the computation domain 4 and 16 that give, after rescaling to the liquid layer, aspect ratio ranges 5–9 and 18–36, respectively. Again, the grid resolution varies with the Rayleigh number. The highest resolution cases contain 512×256 grid cells for the aspect ratio 4 and 1024×128 for the aspect ratio 16. In all experiments we independently verify that at steady state the heat flux balance is satisfied, i.e. the difference between the top and bottom heat flux does not exceed one percent. The bottom boundary is assumed to have a zero shear stress and a fixed temperature. The top of the cavity is a no-slip boundary with a constant temperature. Vertical walls are periodic. The initial temperature profile is isothermal plus top and bottom boundary layers, and a superimposed small random noise. Initial states for high Rayleigh number cases are derived from low Rayleigh number cases.

Fig. 18 shows snapshots of the temperature field for steady and unsteady flows. At stationary state, Fig. 18a, c and e, when variables such as mean temperature and heat fluxes remain constant with time, hot plumes are centred below the highest points of the corrugated interface. This occurs at small Rayleigh numbers. At higher $\mathrm{Ra}_{\mathrm{eff}}$, convection is oscillatory. Boundary layer instabilities develop periodically and are dragged by the main flow around convective cells (Krishnamurti, 1970b; Jarvis, 1984). Variables then oscillate evenly around a mean value.

At even higher $\mathrm{Ra}_{\mathrm{eff}}$, convection is unsteady and non-periodic, Fig. 18f, and variables oscillates irregularly around an average. A

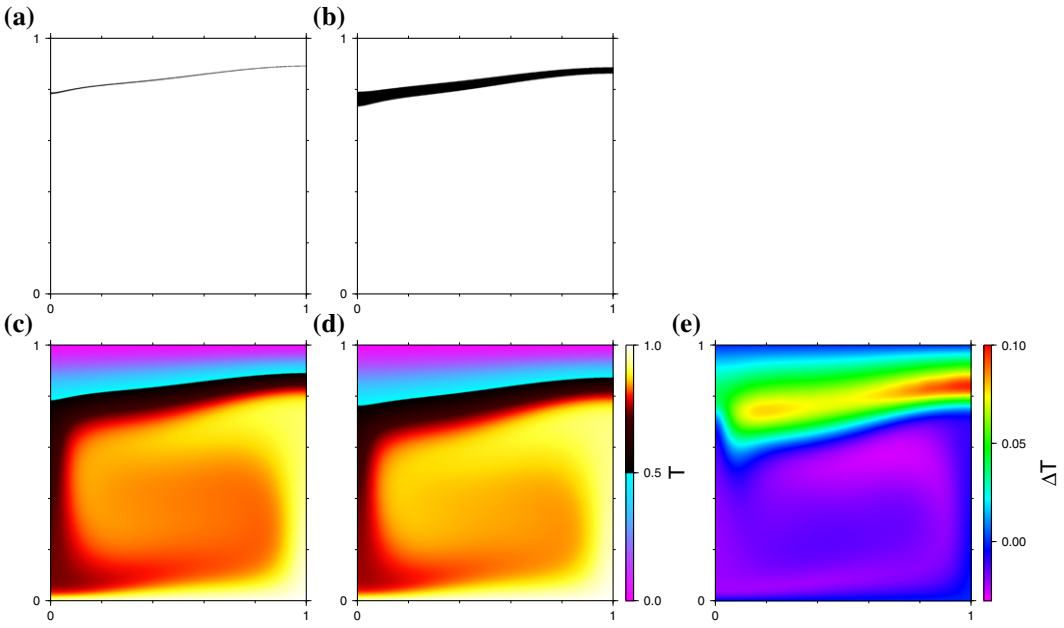

Fig. 16. Influence of the width of the phase change interval for the code using the enthalpy method. Interval where phase change occurs (a) $\epsilon = 0.005$, (b) $\epsilon = 0.05$. (c)–(d) corresponding temperature fields at steady state. (e) difference between the two temperature solutions. (Case with $\mathrm{Pr} = \infty, \mathrm{Ra} = 3 \times 10^5, \mathrm{St} = 0.1$.)

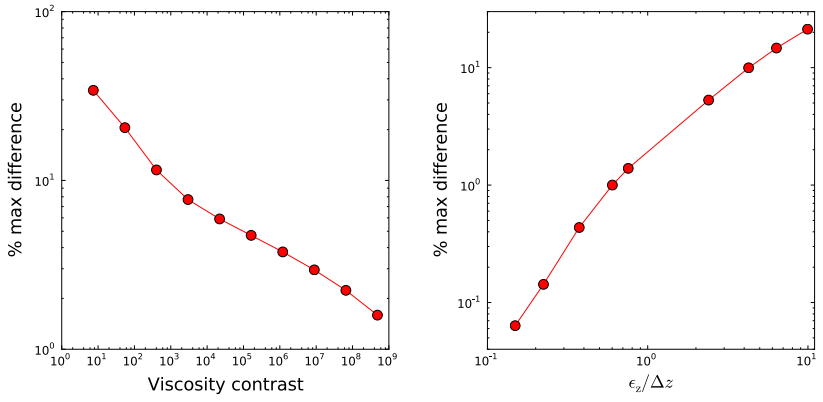

(a) Reference solution with $B = 13$ (corresponds to viscosity contrast $2 \cdot 10^{11}$)

(b) Reference solution with $\epsilon = 0.001$.

Fig. 17. Maximum difference between the temperature and that of a reference solution as a function of (a) the viscosity ratio between the solid and the liquid and (b) phase change width. The mesh step is fixed for all experiments, $\Delta z = 0.0078125$ (corresponds to grid with 128×128 cells).

cluster of hot plumes forms at the bottom boundary drifting horizontally toward the main upwelling. Correspondingly, a set of cold instabilities is forming in the upper boundary layer. Progressive remelting and resolidification thus happens over a broad region where the clusters exist.

Each transition in convective style is generally accompanied by an abrupt change in the heat transfer (Malkus, 1954). The Rayleigh number at which this change occurs depends on the particular setting. In our experiments conducted at $\mathrm{Pr} = 7$ the convection regime changes from steady to oscillating at $\mathrm{Ra}_{\mathrm{eff}} \sim 4 \times 10^4$. Such a sharp transition is not observed for experiments at high Prandtl number and steady and oscillatory experiments are treated together. A second transition to unsteady non-periodic flow happens at $\mathrm{Ra}_{\mathrm{eff}} \sim 10^5$ for $\mathrm{Pr} = 7$ and $\mathrm{Ra}_{\mathrm{eff}} \sim 10^6$ for infinite Prandtl.

We perform a systematic study for $\mathrm{Ra}_{\mathrm{eff}}$ between 10^4 and 10^8. A least squares fit in the form $\mathrm{Nu}_{\mathrm{eff}} = \beta_1 \mathrm{Ra}_{\mathrm{eff}}^{\beta_2}$ is then applied for each of the regimes separately (Fig. 19). Coefficients β_1 and β_2 depend on the style of convection and physical parameters of the system (Pr). β_1 is around 0.2, and the exponent β_2 varies between 0.26 and 0.30 (Table 1).

6.2. Heat transfer and thermal evolution of the basal magma ocean (BMO)

Seismic ultra low velocity zones (ULVZ) at the bottom of the mantle have been detected for more than a decade now (Williams and Garnero, 1996; McNamara et al., 2010). These regions are non homogeneously distributed, have a variable thickness (5–40 km) and could consist of partial melt (Williams and Garnero, 1996). One scenario for their existence is that these zones are the remnants of the thick magma ocean that formed between the mantle and the core early after the Earth was formed and slowly solidified since (Labrosse et al., 2007). Using our parametrization of heat

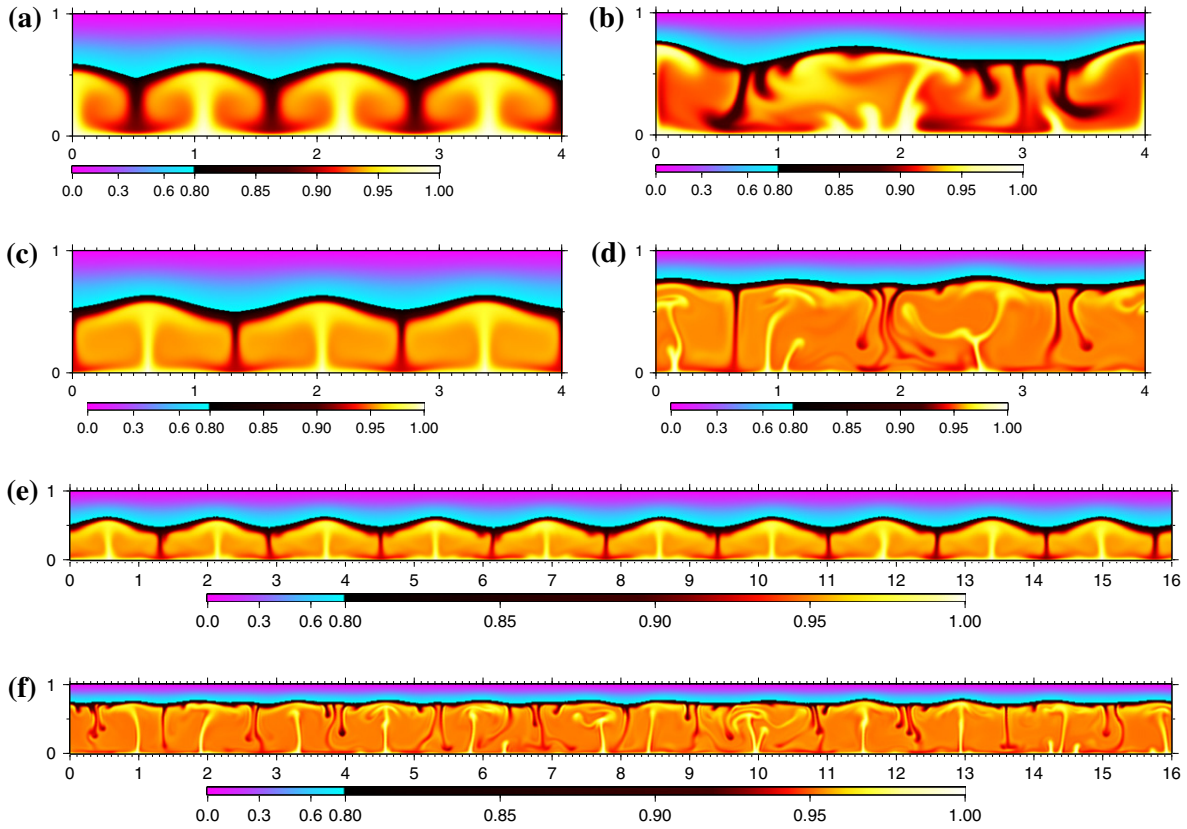

Fig. 18. Snapshots of temperature field in Rayleigh–Bénard convection coupled with solidification/melting at two different Prandtl numbers and different Rayleigh numbers (a) $Pr = 7, Ra_{eff} = 3 \times 10^4$ $(Ra = 9.6 \times 10^5)$; (b) $Pr = 7, Ra_{eff} = 4 \times 10^5$ $(Ra = 6.4 \times 10^6)$; (c) $Pr = \infty, Ra_{eff} = 4 \times 10^5$ $(Ra = 10^7)$ (d); $Pr = \infty, Ra_{eff} = 8 \times 10^6$ $(Ra = 10^8)$; (e) $Pr = \infty, Ra_{eff} = 3 \times 10^5$ $(Ra = 10^7)$ (f); $Pr = \infty, Ra_{eff} = 8 \times 10^6$ $(Ra = 10^8)$.

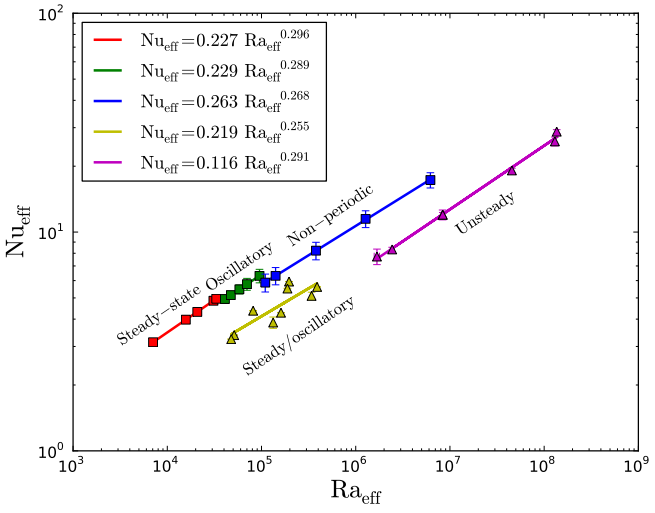

Fig. 19. Effective Nusselt number as a function of the effective Rayleigh number. Two Prandtl numbers are used: Pr = 7 (square symbols) and infinite Prandtl (triangles). Different colors correspond to different convection styles observed. Change from steady to oscillating and unsteady flow is accompanied by the jump in the heat transfer. Lines are the least squares fits obtained for each convecting regime.

transfer developed in the previous subsection we infer the impact of the presence of the BMO on the thermal history of the Earth.

To obtain the typical value of the Stefan number, cf. Eq. (7), we need the estimation of ΔT_t, the total temperature difference over the solid and the liquid. As we show below, high convective vigor of the liquid layer maintains a small temperature difference across it. Thus ΔT_t is approximately equal to the temperature jump over the mantle boundary layer that is around 1000 K. Using this value results in a Stefan number of the order of unity. This implies that timescales of resolidification/remelting are short and the system adjusts nearly instantly to the position of the hot/cold plumes.

Combining Eqs. (21) and (22) for the Nusselt and Rayleigh numbers, together with the fitting relation, we obtain

$$Q = \beta_1 k \left(\frac{\alpha g \rho_0}{\kappa \eta_L}\right)^{\beta_2} (h)^{3\beta_2 - 1} \Delta T_L^{1+\beta_2}, \tag{23}$$

where coefficients β_1 and β_2 were determined experimentally (Table 1). Since β_2 is close to 1/3, the expression is only weakly sensitive to the depth of the liquid layer $\langle h \rangle$.

Eq. (23) is used to determine the temperature jump ΔT_L, which embodies the super-isentropic temperature difference across the BMO. In order to estimate its value, we use parameters listed in Table 2. The most critical but uncertain parameter determining the dynamics of the whole system is the viscosity. There are no experimental results for the viscosity at the pressure conditions pertaining to the bottom of the mantle and extrapolations are not reliable since the pressure effects are nonmonotonic (Liebske et al., 2005). It is assumed that it can be very low, varying between 10^{-2} and 1 Pa s (Solomatov, 2007). Hence, the Prandtl number is between unity and several thousand and Ra_{eff} exceeds 10^{16}. Due to high convective vigor it is appropriate to use the values of coefficients β_1 and β_2 derived for unsteady flow. This results in ΔT_L lower than 0.1 K for $Q = 100\,\mathrm{mW\,m^{-2}}$. Hence, the superisentropic temperature difference maintained across the top and the bottom boundary layers of the BMO is minute and the temperature of the core follows

Table 1
Least squares fitting of equation $Ra_{eff} = \beta_1 Nu_{eff}^{\beta_2}$.

Regime	Pr	β_1	Standard deviation	β_2	Standard deviation
Steady	7	0.227	0.0005	0.296	0.0005
Oscillating	7	0.229	0.0009	0.289	0.0008
Unsteady	7	0.258	0.0023	0.270	0.0016
Steady/oscillating	∞	0.219	0.0658	0.255	0.0583
Unsteady	∞	0.116	0.0066	0.291	0.0079

Table 2
Typical values of the basal magma ocean properties.

Variable	Notation	Value	Unit
Gravitational acceleration	g	10	$m\ s^{-2}$
Density	ρ_0	5500	$kg\ m^{-3}$
Viscosity range	η_L	$10^{-2} - 1$	Pa s
Coefficient of thermal expansion	α	10^{-5}	K^{-1}
Thermal diffusivity	κ	10^{-6}	$m^2\ s^{-1}$
Heat flux into the solid mantle	Q	50–150	$mW\ m^{-2}$

the evolution of the liquidus temperature at the bottom of the mantle. The rate at which the BMO cools is approximately the same as that of the Earth's core, which explains why it can be maintained for so long.

7. Conclusions

We have presented and tested two approaches to compute the evolution of convection with a solid–liquid phase transition. The moving grid method involves explicit tracking of the phase change interface position at each time. We have implemented it in the finite element code Elmer presented here to the geodynamics community. The melting/freezing front is assigned to nodes that follow its motion, deforming the whole mesh. It demands that the topology of the phase transition stays approximately aligned along one of the axes, so that a bijection between the phase change position and the coordinate always exists. This method is particularly suited for simulations with large Stefan number, in which the front is moving slowly and continuously compared to simulations with low Stefan number where quick jumps between two consecutive timesteps can exist.

We also implemented a fixed grid method, called the enthalpy method, in the 3D finite volume code StagYY. In this case, the solid and the liquid, respectively, are treated together in a single non-deforming domain and the latent heat effects are implicitly included in the enthalpy variable. To account for the phase change, suitable functions depending on temperature must be prescribed to describe the liquid phase fraction and the viscosity. Because an abrupt change of material properties is difficult to model with such a method, a transition zone of a given width has to be introduced. This drawback can turn into a benefit if the considered material is not a pure pole. Indeed, a system with multiple components involves a mushy zone (Worster, 1997) which is approximately modeled through the zone of transition between the solid and the liquid. Compositional effects associated with the crystallization of multi-component systems are important for the dynamics of both the mushy layer and the liquid but were not addressed in this simplifying first approach. They should be included in the future.

The phase transformation is incorporated by modifying the heat capacity that, due to temperature dependence, is non-constant. For a given grid, the accuracy of the solution can be enhanced by increasing the viscosity ratio between the solid and the liquid, which is ultimately needed to prevent deformation of the solid, thus limiting the velocities in the mushy region. However, large viscosity gradients are numerically challenging and also significantly increase the computational time.

Both moving and fixed grid codes display a good agreement in the benchmark tests.

We have used the two numerical tools to derive scaling laws for the heat flux as a function of the Rayleigh number in the molten region of the two-phase system, depending on the convective vigor. We have applied the scaling law for unsteady flow to determine the temperature contrast between the base of the mantle and core in the presence of a deep magma ocean. We found that the temperature difference across the top and bottom boundary layers of the BMO is lower than 0.1 K, hence negligible, implying that the potential temperatures at the top of the core for both the BMO and core are equal, therefore the BMO and core cool at the same rate.

Acknowledgments

This work has been supported by the Agence Nationale de la Recherche (DynBMO, ANR-08-JCJC-0084-01). We thank for the constructive comments of an anonymous reviewer and the editor, Mark Jellinek. The authors thank the Pôle Scientifique de Modélisation Numérique (PSMN) for its computing time.

Appendix A. Supplementary data

Supplementary data associated with this article can be found, in the online version, at http://dx.doi.org/10.1016/j.pepi.2012.06.008.

References

Alboussière, T., Deguen, R., Melzani, M., 2010. Melting-induced stratification above the Earth's inner core due to convective translation. Nature 466, 744–747.
Baiocchi, C., Brezzi, F., Franca, L.P., 1993. Virtual bubbles and Galerkin-least-squares type methods (Ga.L.S.). Comput. Meth. Appl. Mech. Engrg. 105, 125–141.
Bertrand, O., Binet, B., Combeau, H., Couturier, S., Delannoy, Y., Gobin, D., Marcel Lacroix, M., Le Quéré, P., Médale, M., Mencinger, J., Sadat, H., Vieira, G., 1999. Melting driven by natural convection A comparison exercise: first results. Int. J. Therm. Sci. 38, 5–26.
Brandeis, G., Jaupart, C., 1986. On the interaction between convection and crystallization in cooling magma chambers. Earth Planet. Sci. Lett. 77, 345–361.
Brandeis, G., Marsh, B.D., 1989. The convective liquidus in a solidifying magma chamber: a fluid dynamic investigation. Nature 339, 613–616.
Christensen, U.R., Yuen, D.A., 1985. Layered convection induced by phase transitions. J. Geophys. Res. 901, 10291.
Coltice, N., Moreira, M., Hernlund, J., Labrosse, S., 2011. Crystallization of a basal magma ocean recorded by Helium and Neon. Earth Planet. Sci. Lett. 308, 193–199.
Crank, J., 1984. Free and Moving Boundary Problems. Oxford University Press, Oxford, UK, pp. 424.
Crank, J., Nicolson, P., 1947. A practical method for numerical evaluation of solutions of partial differential equations of the heat-conduction type. Proc. Cambridge Philos. Soc. 43, 50–67.
CSC – IT Center for Science, 2010. <http://www.csc.fi/english/pages/elmer>.
Davaille, A., Jaupart, C., 1993. Transient high-Rayleigh-number thermal convection with large viscosity variations. J. Fluid Mech. 253, 141–166.
Davies, D.R., Wilson, C.R., Kramer, S.C., 2011. Fluidity: a fully unstructured anisotropic adaptive mesh computational modeling framework for geodynamics. Geochem. Geophys. Geosyst. 120, 6001.
Davis, S.H., 2001. Theory of Solidification. Cambridge University Press, New York, 400 pp.
Davis, S.H., Muller, U., Dietsche, C., 1984. Pattern selection in single-component systems coupling Bénard convection and solidification. J. Fluid Mech. 144, 133–151.
Davis, T.A., 2004. A column pre-ordering strategy for the unsymmetric-pattern multifrontal method. ACM Trans. Math. Softw. 30, 165–195.
Deubelbeiss, Y., Kaus, B.J.P., 2008. Comparison of Eulerian and Lagrangian numerical techniques for the Stokes equations in the presence of strongly varying viscosity. Phys. Earth Planet. Inter. 171, 92–111.
Donea, J., Huerta, A., Ponthot, J.P., Rodríguez-Ferran, A., 2004. Arbitrary Lagrangian–Eulerian methods. In: Stein, E., De Borst, R., Hughes, T.J.R. (Eds.), Encyclopedia of Computational Mechanics (volume 1: Fundamentals), pp. 413–437 (Chapter 14).

Franca, L.P., Frey, S.L., 1992. Stabilized finite element methods: II. The incompressible Navier–Stokes equations. Comput. Meth. Appl. Mech. Engrg. 99, 209–233.
Franca, L.P., Frey, S.L., Hughes, T.J.R., 1992. Stabilized finite element methods: I. Application to the advective–diffusive model. Comput. Meth. Appl. Mech. Engrg. 95, 253–276.
Gobin, D., Le Quéré, P., 2000. Melting from an isothermal vertical wall. Synthesis of a numerical comparison exercise. Comp. Ass. Mech. Eng. Sci. 7, 289–306.
Hughes, T.J.R., 1987. The Finite Element Method. Prentice Hall Inc., Englewood Cliffs, NJ, 803 pp.
Jarvis, G.T., 1984. Time-dependent convection in the Earth's mantle. Phys. Earth Planet. Inter. 36, 305–327.
Jellinek, A.M., Kerr, R.C., 2001. Magma dynamics, crystallization, and chemical differentiation of the 1959 Kilauea Iki lava lake, Hawaii, revisited. J. Volcan. Geotherm. Res. 110, 235–263.
Krishnamurti, R., 1970a. On the transition to turbulent convection. Part 1. The transition from two- to three-dimensional flow. J. Fluid Mech. 42, 295–307.
Krishnamurti, R., 1970b. On the transition to turbulent convection. Part 2. The transition to time-dependent flow. J. Fluid Mech. 42, 309–320.
Labrosse, S., Hernlund, J.W., Coltice, N., 2007. A crystallizing dense magma ocean at the base of the Earth's mantle. Nature 450, 866–869.
Liebske, C., Schmickler, B., Terasaki, H., Poe, B.T., Suzuki, A., Funakoshi, K.I., Ando, R., Rubie, D.C., 2005. Viscosity of peridotite liquid up to 13 GPa: implications for magma ocean viscosities. Earth Planet. Sci. Lett. 240, 589–604.
Malkus, W.V.R., 1954. Discrete transitions in turbulent convection. Proc. R. Soc. Lond. A 225, 185–195.
McNamara, A.K., Garnero, E.J., Rost, S., 2010. Tracking deep mantle reservoirs with ultra-low velocity zones. Earth Planet. Sci. Lett. 299, 1–9.
Notz, D., Worster, M.G., 2006. A one-dimensional enthalpy model of sea ice. Ann. Glaciol. 44, 123–128.
Schmeling, H., Babeyko, A.Y., Enns, A., Faccenna, C., Funiciello, F., Gerya, T., Golabek, G.J., Grigull, S., Kaus, B.J.P., Morra, G., Schmalholz, S.M., van Hunen, J., 2008. A benchmark comparison of spontaneous subduction models – towards a free surface. Phys. Earth Planet. Inter. 171, 198–223.
Solomatov, V., 2007. Magma oceans and primordial mantle differentiation. In: Schubert, G. (editor-in-chief) and Stevenson, D. (volume editor). Treatise on Geophysics: Evolution of the Earth, vol. 9. Elsevier Ltd., pp. 92–119.
Tackley, P.J., 1993. Effects of strongly temperature-dependent viscosity on time-dependent, three-dimensional models of mantle convection. Geophys. Res. Lett. 20, 2187–2190.
Tackley, P.J., 1996. Effects of strongly variable viscosity on three-dimensional compressible convection in planetary mantles. J. Geophys. Res. 101, 3311–3332.
Tackley, P.J., 2002. Strong heterogeneity caused by deep mantle layering. Geochem. Geophys. Geosyst. 3.
Tackley, P.J., 2008. Modelling compressible mantle convection with large viscosity contrasts in a three-dimensional spherical shell using the yin-yang grid. Phys. Earth Planet. Inter. 171, 7–18.
Taylor, C., Hood, P., 1973. Numerical solution of the Navier–Stokes equations using the finite element technique. Comput. Fluids 1, 1–28.
Viswanath, R., Jaluria, Y., 1993. A comparison of different solution methodologies for melting and solidification problems in enclosures. Numer. Heat Transf. B 24, 77–105.
Voller, V.R., 1985. Implicit finite difference solutions of the enthalpy formulation of Stefan problems. IMA J. Numer. Anal. 5, 201–214.
Voller, V.R., 1996. An overview of numerical methods for solving phase change problems. In: Minkowycz, W.J., Sparrow, E.M. (Eds.), Advances in Numerical Heat Transfer, vol. 1. pp. 341–375 (Chapter 9).
Voller, V.R., Swaminathan, C.R., Thomas, B.G., 1990. Fixed grid techniques for phase change problems: a review. Int. J. Numer. Meth. Engrg. 30, 875–898.
Van der Vorst, H.A., 1992. Bi-CGSTAB: A fast and smoothly converging variant of Bi-CG for the solution of nonsymmetric linear systems. SIAM J. Sci. Stat. Comp. 13, 631–644.
Williams, Q., Garnero, E.J., 1996. Seismic evidence for partial melt at the base of Earth's mantle. Science 273, 1528–1530.
Worster, M.G., 1997. Convection in mushy layers. Ann. Rev. Fluid. Mech. 29, 91–122.
Worster, M.G., Huppert, H.E., Sparks, R.S.J., 1993. The crystallization of Lava lakes. J. Geophys. Res. 98, 15891–15901.